Short Communication

Antimony-doped SnO₂ hollow nanospheres as negative materials for high-performance lithium-ion batteries

Sai Wang[1], Jianxiong Liu[1], Xiaohua Yu[1], Yingjie Zhang[1,2], Jiaming Liu[3], Zhongren Zhong[2], Zhaolin Zhan[1], Mingyu Zhang[4], Xi Yang[4], Peng Dong[2,*], Yannan Zhang[2,*]

[1] Faculty of Materials Science and Engineering, Kunming University of Science and Technology, Kunming 650093, China
[2] National and Local Joint Engineering Laboratory for Lithium-ion Batteries and Materials Preparation Technology, Key Laboratory of Advanced Battery Materials of Yunnan Province, Faculty of Metallurgical and Energy Engineering, Kunming University of Science and Technology, Kunming 650093, China
[3] School of Metallurgy Engineering, Jiangxi University of Science and Technology, Ganzhou 341000, China
[4] Yunnan Provincial Energy Research Institute Co., LTD., Kunming 650093, China
[*]E-mail: dongpeng2001@126.com (Peng Dong), zyn_legolas@163.com (Yannan Zhang)

SnO_2-based lithium-ion batteries suffer from capacity fades rapidly during lithiation and delithiation at high current density due to the aggregation and cracking of active materials. This work proposes a novel architecture of antimony-doped SnO_2 (ATO) hollow nanospheres using hydrothermal and hard template methods. The crystal structure, morphology, and surface elemental composition of ATO are tested by XRD, SEM TEM and XPS, respectively. Notably, the electrochemical tests results indicate that the ATO negative materials exhibit a significantly improved cycling and rate performance than that pure hollow SnO_2 nanospheres. After 100 cycles, ATO still maintains a high capacity retention of 709 mAh g^{-1} at 0.1 A g^{-1} and delivers 286 mAh g^{-1} even at 5 A g^{-1}. These consequences reveal that the Sb modified SnO_2 hollow sphere electrodes have good implications for the design of high-power-density negative materials of the next-generation lithium-ion batteries.

1. INTRODUCTION

Transmission metal oxide such as SnO_2, Co_3O_4 and Fe_3O_4 have been regarded as promising candidate for graphite anode because they have much higher specific capacity than graphite [1-5]. Among these materials, SnO_2 shows attractive characteristics as the negative materials of LIBs for its

high volume density of 6.5g cm^{-3}, high theoretical capacity ($\approx$782 mAh g^{-1}), safe working potential ($\approx$0.6 V vs Li$^+$/Li), and low cost [6-9].

Unfortunately, SnO$_2$-based electrodes have some fatal weaknesses owing to large irreversible reaction and the huge volume expansion that accompany the lithium-ion insertion/extraction process [10-12]. The repeated volume expansion/contraction results in severe stress that may easily cause the pulverization and agglomeration of electrode, which finally leads to rapid irreversible capacity fading and thermal run-away during long-term cycling [13]. The intrinsic conductivity of SnO$_2$ is poor with a wide energy bandgap (E$_g$ = 3.62 eV) which is another reason of poor cycling performance and rate capability [14, 15].

To overcome the poor durability and boost the cycling stability of SnO$_2$-based electrodes, several modification strategies such as hollow structural fabrication have been reported [10, 16, 17]. The shortened diffusion pathway for electron and Li$^+$, and empty interior space provide better conductivity and cycling stability than other nanostructures [18]. However, although the hollow SnO$_2$ nanospheres can improve SnO$_2$ based anode electrochemical performance to some extent, SnO$_2$ still has the possibility of cracking, aggregation, and collapse after long-term cycles at high current density. Elemental doping is an effective strategy to increase the intrinsic conductivity of SnO$_2$, several modification strategies have been reported [19]. Wang et al. prepared Mo-doped with 16 at% Mo doping SnO$_2$ hollow spheres, which display a favorable specific capacity of 525 mAh g^{-1} after 60 cycles at a current density of 100 mA g^{-1} [20]. Ma et al. obtained Co-doped SnO$_2$ nanoparticles through sol-gel methode, which also exhibit favorable electrochemical performance of 493 mAh g^{-1} under 100 mA g^{-1} after 50 cycles [21].

As we all know, SnSb alloys is a typical intermetallic compound containing two lithium reaction centers and is considered to be one of the most intermetallic compounds with lithium storage prospects [15, 22]. Therefore, the antimony doping has a positive effect on Sn-based negative material performance. Herein, we have fabricated a hollow nanospheres of antimony-doped SnO$_2$ (ATO) through a facile hydrothermal method which may further prevent the issues associated with cracking, aggregation, and collapse of hollow SnO$_2$ nanospheres to some extent. The volume expansion and conductivity are effectively buffered and improved by introducing heteroatoms. Hance, the ATO hollow nanospheres exhibit an outstanding reversible capacity of 709 mAh g^{-1} at 100 mA g^{-1} after 100 cycles, delivers a remarkable rate performance of 286 mAh g^{-1} even at 5 A g^{-1}. Compared with pure tin dioxide hollow nanospheres, the electrochemical performance is significantly improved through antimony doping.

2. EXPERIMENTAL

2.1 Preparation of hollow Sb-doped SnO$_2$ (ATO) nanospheres.

The hollow ATO nanospheres were fabricated by following combined three-step sol-gel process and one-step hydrothermal process. (1) SiO$_2$ templates were prepared by well-known Stöber method [23]. 3.14 mL of 28% ammonia solution was dropped in a mixture of 74 mL ethanol and 10 mL deionized water under stirring for 0.5 h. After that, 6 mL teraethylorthosilicate (TEOS) was injected to the solution,

then the mixture was reacted under 300 rpm stirred 22 h, subsequently, the SiO_2 nanospheres were collected by centrifugation and washed with ethanol 3 times. (2) The as-prepared colloidal SiO_2 nanospheres (0.2 g) were dispersed in a mixture of ethanol (9 mL) and water (19 mL), Then, stannous chloride ($SnCl_2·2H_2O$, 0.12 g), urea (0.9 g) and antimonous chloride ($SbCl_3$, 0.014 g) were added to the suspension, and the suspension continuously stirred for 1 hour. (3) The homogeneous was shifted into a Teflon autoclave and heated at 200ºC for 2 h, yielding SiO_2@ATO nanospheres, the obtained products were annealed at 500ºC for 4 h under air atmosphere. (4) Finally, the SiO_2 nanospheres were etching by HF solution (5%, 40 mL), the ATO hollow spheres were collected and washed with deionized waters for 3 times. The synthesis route of the ATO is schematically illustrated in Figure 1. As a control, the SnO_2 hollow nanospheres (SNO) was fabricated in the same condition without added $SbCl_3$.
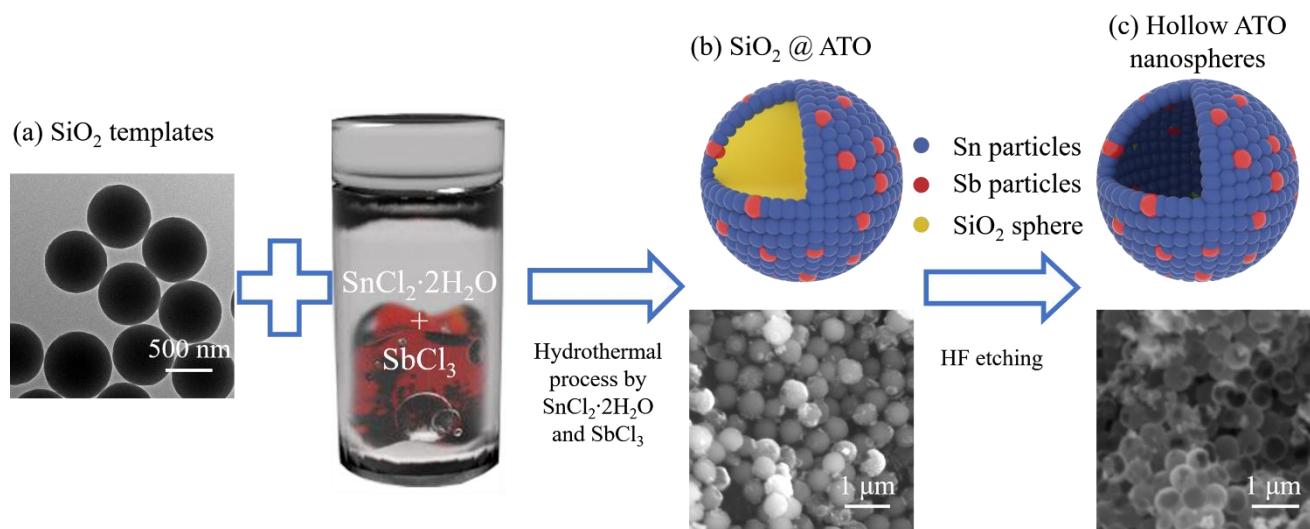
Figure 1. Schematic illustration of the formation of ATO hollow spheres.

2.2 Sample characterization.

The structure of as-prepared products were conducted by X-ray diffraction (XRD, Bruker D8 Advanced X-ray diffraction, Cu Kα radiation (λ=1.5406 Å)). The morphology and microstructure of smaples were examined by transmission electron microscope (TEM, FEI Tecnai G2 F20 S-TWIN) and field-emission scanning electron microscope (FE-SEM, LEO 1530Vp). The valence state of ATO and SNO were determined through X-ray photoelectron spectroscopy (XPS, PHI5000 Versaprobe-II).

2.3 Electrochemical Measurements.

The electrochemical properties of the ATO and SNO as a negative material for LIBs were explored through the CR2025-type coin cells. Pure lithium metal was used as the counter electrode. The working electrodes were composed of the 80% active material, 10% acetylene black and 10% polyvinylidene (PVDF). The electrolyte was $LiPF_6$ (1M) in a mixed solution of dimethyl carbonate (DC), ethylene methyl carbonate (EMC), and ethylene carbonate (EC) (1:1:1 by volume). All of these composites were packaged in a glovebox among argon atmosphere. Charge-discharge characteristics were conducted by LAND CT-3008 battery tester (Wuhan, China), the cycling performance and rate

capability were carried out in the same tester with a voltage range of 0.05 and 3 V at different current density from 0.1 A g^{-1} to 5 A g^{-1}. Electrochemical impedance spectroscopy (EIS) was implemented on CHI 660D electrochemical workstation in the frequency range from 100 kHz to 0.01 Hz with an amplitude of 5 mV.

3. RESULTS AND DISCUSSION

The crystallographic properties of the ATO, SNO hollow nanospheres was conducted by X-ray diffraction (XRD) and The results are shown in Figure 2a. The diffraction peaks of the SNO sample presents a typical tetragonal rutile SnO_2 (PDF 41-1445) [24-26]. After Sb doping, the crystal structure of SnO_2 is not changed. The XRD patterns of the SNO, ATO samples are basically in agreement with that of tetragonal rutile SnO_2, and no other obvious peaks of impurities are detected such as Sb oxides (Sb_2O_3, Sb_2O_5) [27]. Figure 2b presents the magnified (110) diffraction peak of ATO samples, it can be clearly seen that the (110) peak shifts to the larger angles. The reason for the Sb incorporation into SnO_2 causing the decrease in lattice constant is since the smaller radius of the Sb^{5+} ion (0.62 Å) than that of the Sn^{4+} (0.69 Å) ion [25]. The XRD results indicate that Sb was successfully incorporated into the SnO_2 lattice.
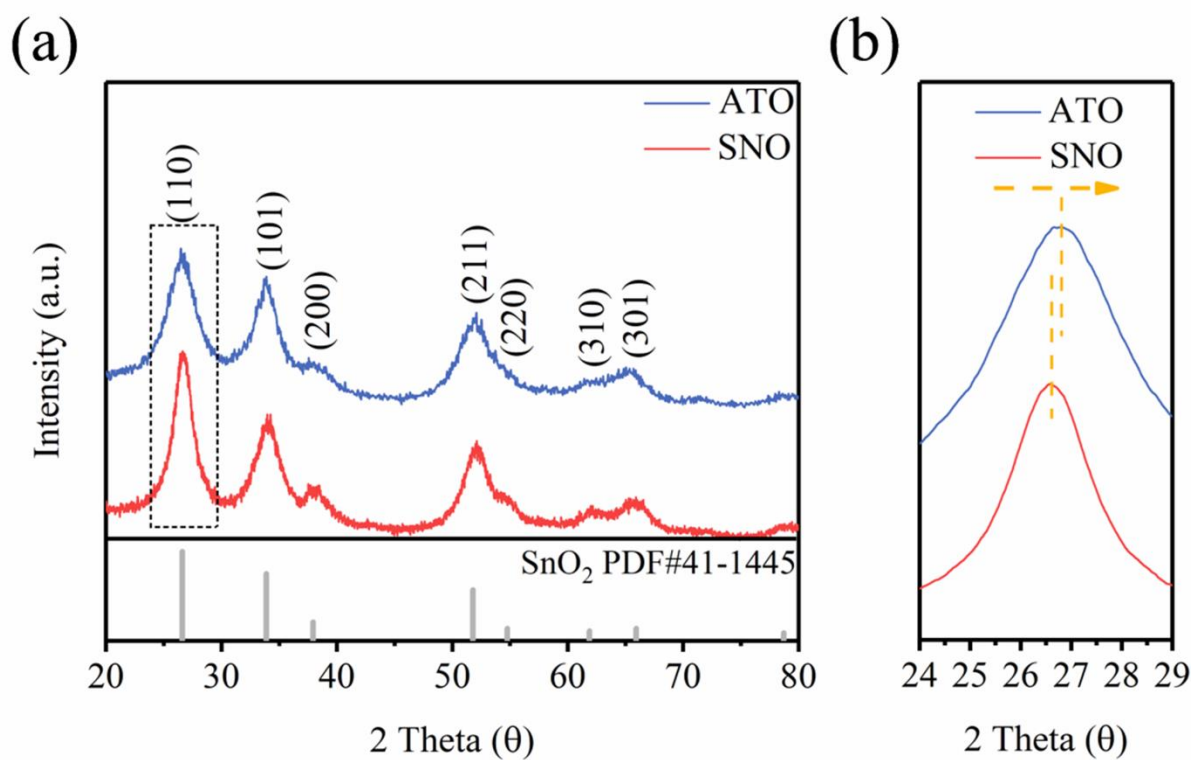
Figure 2. (a) XRD pattern of ATO, SNO hollow nanospheres, (b) high-resolution (110) peak of two samples.

To further investigate the valence state of Sn, Sb and O in ATO samples, XPS has been employed

to analyze all composites, as shown in Figure 3. The wide survey spectra of as-prepared anode materials are given in Figure 3a. The XPS spectrum indicate that the ATO involves only the O, Sn and Sb elements. Figure 3b-c present the high-resolution XPS spectra of individual elements. Figure 3b plots the XPS spectrum of Sn 3d, the two symmetric peaks located at 487.5 and 495.9 eV can be attributed to Sn $3d_{3/2}$ and Sn $3d_{5/2}$ lines [28], respectively. The values indicate the presence of the Sn^{4+}. Interestingly, an negative shift with approximately 0.2 eV in the sample of ATO indicates a lower binding energy according to less O around the Sn [29]. Figure 3c shows the XPS spectrum of O 1s and Sb 3d of the two samples. Although the Sb 3d peaks were partially coincides with that of O 1s, the spectrum of Sb 3d were easily identified through deconvolution of O 1s peak. The Sb $3d_{5/2}$ and Sb $3d_{3/2}$ are assigned to binding energies 531 and 540.3 eV, respectively, which exhibited that the largest fraction of Sb has a valency of 5^+ [27, 30]. In addition, the existence of Sb^{5+} will increase the concentration of free electron in SnO_2 nanocrystals, thus contributing to the electrical conductivity of bulk materials [31].
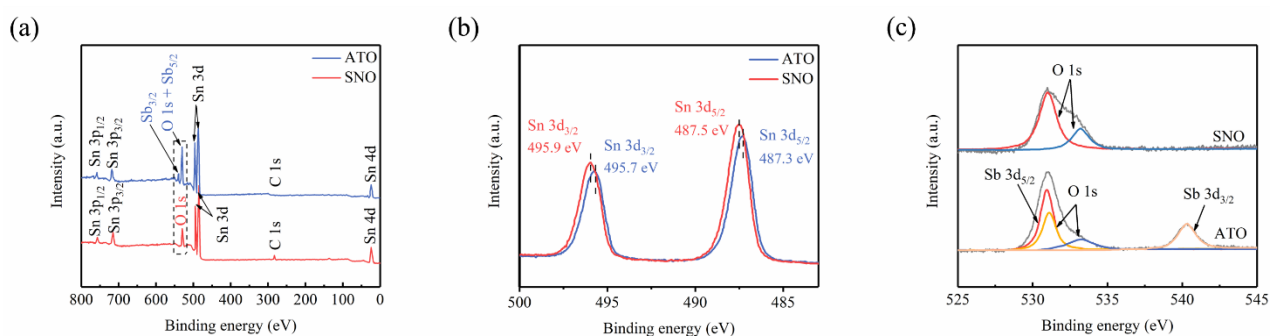
Figure 3. (a) XPS survey spectra of the ATO, SNO hollow nanospheres. (b) Sn 3d XPS spectra of ATO and SNO hollow nanospheres (c) Sb 3d XPS spectra of ATO, SNO hollow nanospheres.

To explore the morphology and microstructure of the as-prepared samples, the FESEM and TEM characterization were conducted. as shown in Figure 4. Figure 4a presents the FESEM image of ATO, and we can seen the sample has a uniform spherical structure from 360-380 nm with a smooth surface. To further investigate the inner structure of ATO, the TEM images in Figure 4b were captured to further confirm that with hollow nanosphere structure of the ATO samples., the thickness of the shell is approximately 30 nm. In the magnified image (inset Figure 4b), clear lattice fringes with a d-spacing of 0.335 nm are detected and can be ascribed to the (110) plane of rutile SnO_2 (JCPDS card No. 41-1445) [7, 32].
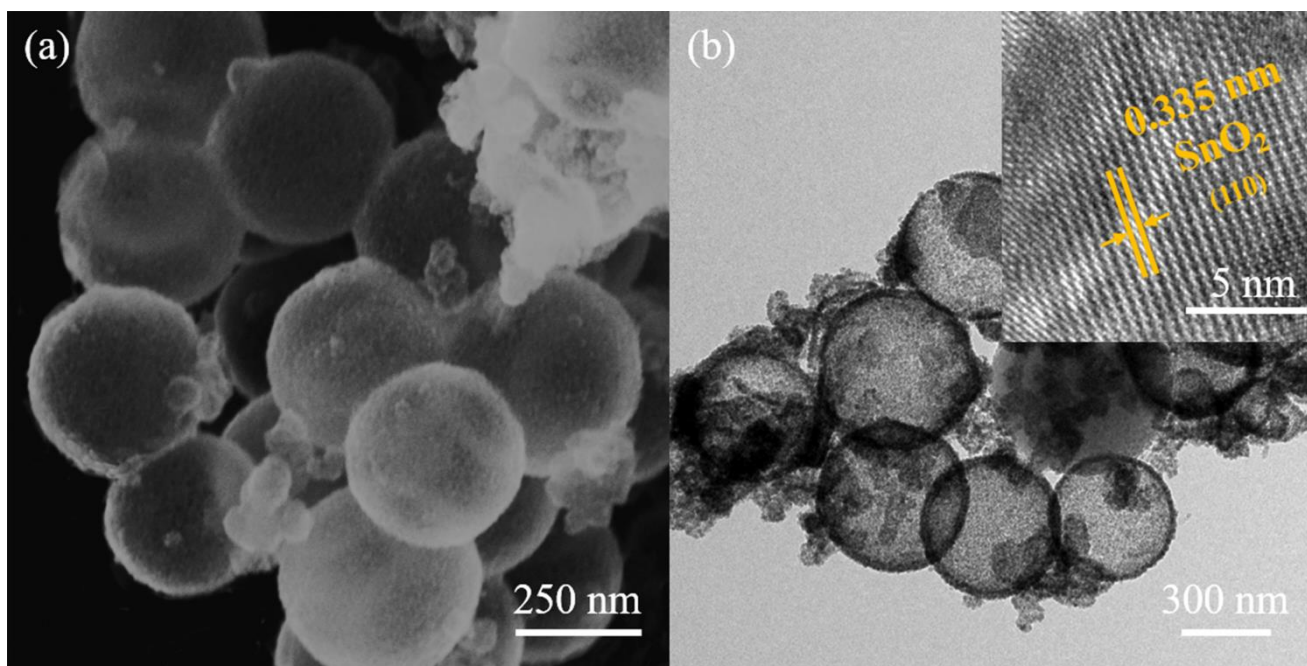
Figure 4. (a) FE-SEM image of ATO hollow nanospheres. (b) TEM image of ATO hollow nanospheres. Inset in part c is the HRTEM image of ATO hollow spheres.

To further evaluate the cycling stability and rate performance, galvanostatic technique was carried out. Figure 5a, b shows the 1st, 2nd, 10th, 20th and 30th charge/discharge performance of the SNO and ATO electrodes at a current density of 0.1 A g^{-1} between 0.05 and 3 V. The initial discharge capacities of SNO and ATO samples are 1521 and 1529 mA h g^{-1}. Both of subsequent discharge and charge-specific capacities of SNO and ATO suffer serious capacity losses. The initial capacity fade is caused mainly by the irreversible reaction of SnO_2 and the Li ions to produce Sn and Li_2O [33, 34]. It's worth noting that the ATO sample displays a higher capacity retention after 30 cycle as compared with that of SNO (735 mAh g^{-1} instead of 618 mAh g^{-1}). This observation results from the positive effects to the charge-discharge stability after Sb doping.
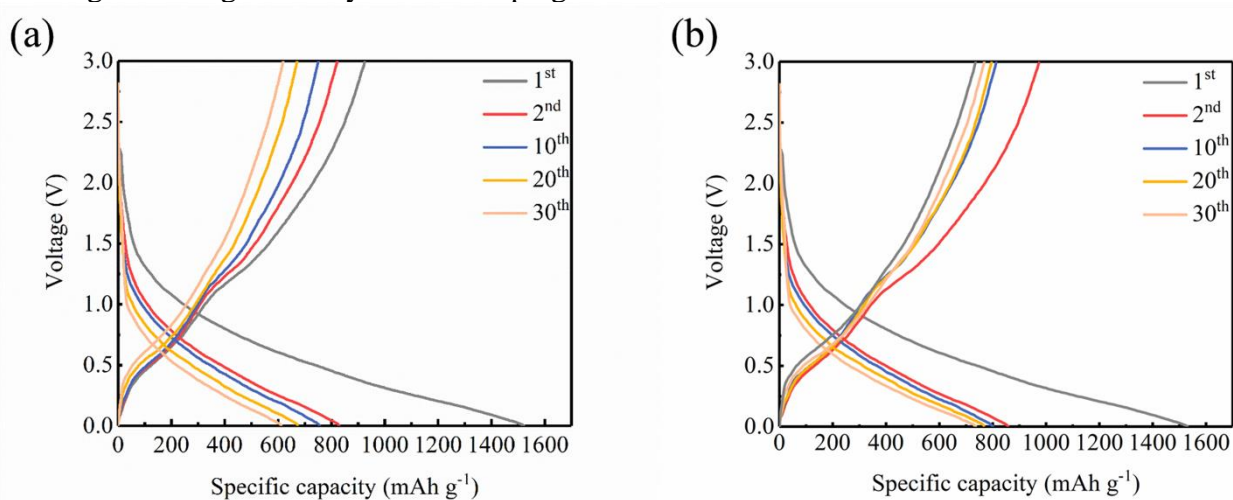
Figure 5. (a) Charge/discharge curves of the ATO hollow spheres at a current density of 100 mA g^{-1}. (b) Charge/discharge curves of the SNO hollow spheres at a current of 100 mA g^{-1}.

Figure 6a shows the cycling performance of the SNO and ATO at a galvanostatic current density of 0.1 A g^{-1}. It can be seen that the discharge capacity of SNO rapidly decays until 60 th cycle, shows a poor retention rate of only 52% after 100 cycles, while the ATO exhibits a favorable capacity retention of 72.7% up to 100 cycles. Its coulombic efficiency always remains at approximately 100% except for the first cycle. The better cycling performance is because that the Sb react with Li^+ will before the Sn counterpart due to their thermodynamics properties, which is good for keeping the structure integrity of ATO from volume change [15], thereby further improving the lithium storage capability. Moreover, we have compared the capacity retention of ATO hollow nanospheres with some previous reports of SnO_2 based negative materials in LIBs, as shown in Table 1. It is noted that even after 100 cycles, the ATO negative materials exhibit superior reversible capacities to other cationic doped nanostructures.

Table 1. The comparison of the cycling performance with previous literatures of cationic doped SnO_2 negative materials

Sample	Cycle number	Reversible capacities (mAh g^{-1})	Voltage range (V)	Ref
This work	**100**	**709 (80 mA g^{-1})**	**0.05-3 V**	
Mo-doped SnO_2 hollow spheres	60	801 (100 mA g^{-1})	0.01-3 V	[20]
Co-doped SnO_2 nanoparticles	50	493 (100 mA g^{-1})	0.005-3 V	[21]
Co/N-doped SnO_2 nanocrystals	50	716 (80 mA g^{-1})	0.005-3 V	[35]
Al-doped SnO_2 hollow spheres	50	443 (80 mA g^{-1})	0-3 V	[24]
Ni/N-doped SnO_2 Nanoparticles	50	664 (80 mA g^{-1})	0.005-3 V	[36]
CNF/ATO/C	100	705 (100 mA g^{-1})	0.05-3 V	[25]
Sb-doped SnO_2 microspheres	100	194 (80 mA g^{-1})	0.005-3 V	[30]
Ni-doped SnO_2 nanoparticles	35	674 (160 mA g^{-1})	0.05-2 V	[37]
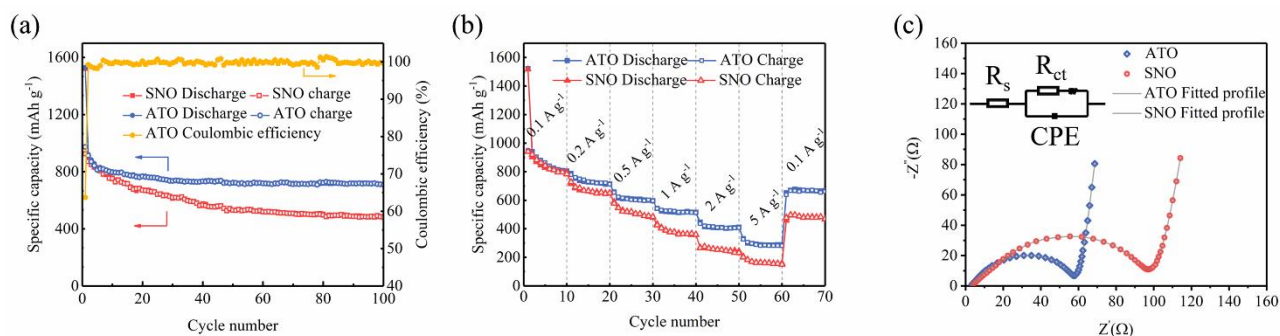
Figure 6. (a) Cycling performances of ATO and SNO samples at a constant current density of 100 mA g^{-1}. (b) Rate performance of ATO hollow spheres and SNO hollow spheres at different current density from 0.1 A g^{-1} to 5 A g^{-1}. (c) Nyquist plots of ATO hollow spheres and SNO hollow spheres.

The rate capabilities of the ATO and SNO at various specific current densities from 100 to 5000 mA g^{-1} are illustrated in Figure 6b. It can be seen that ATO delivers higher retention capacities than that of the SNO at all kinds of current density from 0.1 to 5 A g^{-1}. In particular, the Sb doped sample displays a discharge capacity of 286 mAh g^{-1} at 5 A g^{-1}, which is almost 2 times more than that of the undoped one. The excellent rate and cycling performance of ATO are mainly attributed to Sb doping can significantly improve intrinsic conductivity of SnO$_2$ anode and reduced residual stresses during cycles.

To further explore the kinetics during the electrochemical reaction of ATO and SNO, electrochemical impedance spectroscopy (EIS) was conducted after 5 cycles. As shown in Figure 6c, each of the plots consists of a semicircle in high-medium frequency region, which presents charge transfer impedance (Rct), and the inclined line in the low frequency assigned to lithium-ion diffusion processes [38-40]. The fitting data was inserted in the Table 2. The Ohmic resistance (Rs) of ATO is simulated as 3.3 Ω, which is lower than that of the SNO (4.1 Ω). The calculated charge-transfer resistance of ATO is 28 Ω, which is also lower than that of SNO (47 Ω). The results indicate that the Sb doped SnO$_2$ hollow nanospheres can enhance the electrochemical kinetics and facilitate the lithium ion diffusion.

Table 2. The fitted results of the Ohmic resistance (Rs) and charge transfer impedance (Rct) for ATO and SNO.

Samples	ATO	SNO
Rct(Ω)	28	47
Rs(Ω)	3.3	4.1

4. CONCLUSION

In summary, ATO hollow nanospheres was successfully synthesized through a facile strategy

combined hard template and hydrothermal methods The antimony doping has no obvious effect on the nanosphere morphology. Compared with the undoped SnO_2 samples, the as-prepared ATO electrodes deliver outstanding cycle stability and favorable rate performance, exhibit an outstanding reversible capacity of 709 mAh g^{-1} after 100 cycles and deliver 286 mAh g^{-1} even at 5 A g^{-1}. EIS measurements also show that ATO electrodes have better electrochemical kinetics than that of the undoped one. All results suggest that the antimony doping is an useful strategy to improve electrochemical performance of Sn-based negative materials.

References

1. L. Zu, Q. Su, F. Zhu, B. Chen, H. Lu, C. Peng, T. He, G. Du, P. He, K. Chen, S. Yang, J. Yang and H. Peng, *Adv. Mater.,* 29 (2017) 1701494.
2. H. Xie, M. Chen and L. Wu, *Small,* 13 (2017) 1604283.
3. G. Zhang, Y. Shi, H. Wang, L. Jiang, X. Yu, S. Jing, S. Xing and P. Tsiakaras, *J. Power Sources,* 416 (2019) 118-124.
4. M. Jing, M. Zhou, G. Li, Z. Chen, W. Xu, X. Chen and Z. Hou, *ACS Appl. Mater. Interfaces,* 9 (2017) 9662-9668.
5. L. Liu, F. Xie, J. Lyu, T. Zhao, T. Li and B.G. Choi, *J. Power Sources,* 321 (2016) 11-35.
6. M.G. Park, D.H. Lee, H. Jung, J.H. Choi and C.M. Park, *ACS Nano,* 12 (2018) 2955-2967.
7. W. Guo, Y. Wang, Q. Li, D. Wang, F. Zhang, Y. Yang and Y. Yu, *ACS Appl. Mater. Interfaces,* 10 (2018) 14993-15000.
8. K. Zhao, L. Zhang, R. Xia, Y. Dong, W. Xu, C. Niu, L. He, M. Yan, L. Qu and L. Mai, *Small,* 12 (2016) 588-594.
9. B. Huang, X. Li, Y. Pei, S. Li, X. Cao, R.C. Masse and G. Cao, *Small,* 12 (2016) 1945-1955.
10. J. Liang, X. Y. Yu, H. Zhou, H. B. Wu, S. Ding and X. W. Lou, *Angew. Chem. Int. Edit.,* 53 (2014) 12803-12807.
11. S. Y. Zuo, Z. G. Wu, S. K. Li, D. Yan, Y. H. Liu, F. Y. Wang, R. F. Zhuo, B. S. Geng, J. Wang and P. X. Yan, *RSC Adv.,* 7 (2017) 18054-18059.
12. J. Tang, J. Yang, X. Zhou, H. Yao and L. Zhou, *J. Mater. Chem. A,* 3 (2015) 23844-23851.
13. P. Zhang, S. Zhu, Z. He, K. Wang, H. Fan, Y. Zhong, L. Chang, H. Shao, J. Wang, J. Zhang and C. N. Cao, *J. Alloy. Compd.,* 674 (2016) 1-8.
14. Y. Wang, I. Djerdj, B. Smarsly and M. Antonietti, *Chem. Mater.,* 21 (2009) 3202-3209.
15. J. Cui, S. Yao, J. Q. Huang, L. Qin, W. G. Chong, Z. Sadighi, J. Huang, Z. Wang and J.K. Kim, *Energy Storage Mater.,* 9 (2017) 85-95.
16. B. Cao, Z. Liu, C. Xu, J. Huang, H. Fang and Y. Chen, *J. Power Sources,* 414 (2019) 233-241.
17. T. Ma, X. Yu, H. Li, W. Zhang, X. Cheng, W. Zhu and X. Qiu, *Nano Lett.,* 17 (2017) 3959-3964.
18. Y. N. Zhang, Y. J. Zhang, J. Rong, J. H. Wu, P. Dong, M. L. Xu, J. Feng and C. D. Gu, *J. Alloy. Compd.,* 795 (2019) 177-186.
19. F. Mueller, D. Bresser, V.S.K. Chakravadhanula and S. Passerini, *J. Power Sources,* 299 (2015) 398-402.
20. X. Wang, Z. Li, Z. Zhang, Q. Li, E. Guo, C. Wang and L. Yin, *Nanoscale,* 7 (2015) 3604-3613.
21. Y. Ma, Y. Ma, U. Ulissi, Y. Ji, C. Streb, D. Bresser and S. Passerini, *Electrochim. Acta,* 277 (2018) 100-109.

22. L. W. Li, M. Gu, Y. S. Shao, X. L. Li, M.H. Engelhard, B.W. Arey, W. Wang, Z. M. Nie, J. Xiao, C. M. Wang, J.-Guang. Zhang and J. Liu, *Adv. Mater.,* 26 (2014) 2901-2908.
23. W. Stöber, A. Fink and E. Bohn, *J. Colloid. Interf. Sci.,* 26 (1968) 62-69.
24. C. W. Wei, G. X. Zhang, Y. Bai, D. Yan, C. Y. Yu and N. Wan and W. Zhang, *Solid State Ionics,* 272 (2015) 133-137.
25. G.H. An, D.Y. Lee, Y.J. Lee and H.J. Ahn, *ACS Appl. Mater. Interfaces,* 8 (2016) 30264-30270.
26. C. Miao, M. Liu, Y. B. He, X. Qin, L. Tang, B. Huang, R. Li, B. Li and F. Kang, *Energy Storage Mater.,* 3 (2016) 98-105.
27. P. Ouyang, H. Zhang, Y. Wang, W. Chen and Z. Li, *Electrochim. Acta,* 130 (2014) 232-238.
28. Y. Y. Cheng, J. F. Huang, H. Qi, L. Y. Cao, J. Yang, Q. Xi, X. M. Luo, K. Yanagisawa and J. Y. Li, *Small,* 13 (2017) 1700656.
29. W. Dong, J. Xu, C. Wang, Y. Lu, X. Liu, X. Wang, X. Yuan, Z. Wang, T. Lin, M. Sui, I. W. Chen and F. Huang, *Adv. Mater.,* 29 (2017).
30. Y. Wang and T. Chen, *Electrochim. Acta,* 54 (2009) 3510-3515.
31. K. Peters, P. Zeller, G. Stefanic, V. Skoromets, H. Němec, P. Kužel and D. Fattakhova-Rohlfing, *Chem. Mater.,* 27 (2015) 1090-1099.
32. J. Li, P. Wu, Y. Ye, H. Wang, Y. Zhou, Y. Tang and T. Lu, *CrystEngComm,* 16 (2014) 517-521.
33. V.M.H. Ng, S. Wu, P. Liu, B. Zhu, L. Yu, C. Wang, H. Huang, Z. J. Xu, Z. Yao, J. Zhou, W. Que and L. B. Kong, *Electrochim. Acta,* 248 (2017) 440-448.
34. J. Qin, N. Zhao, C. Shi, E. Liu, F. He, L. Ma, Q. Li, J. Li and C. He, *J. Mater. Chem. A,* 5 (2017) 10946-10956.
35. N. Wan, X. Lu, Y. Wang, W. Zhang, Y. Bai, Y. S. Hu and S. Dai, *Sci. Rep*., 6 (2016) 18978.
36. N. Wan, T. T. Zhao, S. W. Sun, Q. Wu and Y. Bai, *Electrochim. Acta*, 143 (2014) 257-264.
37. 8.   X. M. Ye, W. J. Zhang, Q. J. Liu, S. P. Wang, Y. Z. Yang and H. Wei, *N. J. Chem*., 39 (2015) 130-135.
38. Y. N. Zhang, P. Dong, M. Y. Zhang, X. L. Sun, X. H. Yu, J. Song, Q. Meng, X. Li and Y. J. Zhang, *J. Appl. Electrochem.,* 48 (2017) 135-145.
39. Y. N. Zhang, P. Dong, J. B. Zhao, X. Li and Y. J. Zhang, *Ceram. Int.,* 45 (2019) 11382-11387.
40. Y. N. Zhang, Y. J. Zhang, M. Y. Zhang, M. L. Xu, X. Li, X. H. Yu and P. Dong, *JOM,* 71 (2019) 608-612.